



# Microstructure and performance of Z-scheme photocatalyst of silver phosphate modified by MWCNTs and Cr-doped SrTiO<sub>3</sub> for malachite green degradation

Yan Lin<sup>a,1</sup>, Shaohua Wu<sup>a,1</sup>, Xiang Li<sup>a,1</sup>, Xin Wu<sup>a,1</sup>, Chunping Yang<sup>a,b,\*</sup>, Guangming Zeng<sup>a</sup>, Yanrong Peng<sup>a</sup>, Qi Zhou<sup>a</sup>, Li Lu<sup>b,\*</sup>

<sup>a</sup> College of Environmental Science and Engineering, Hunan University and Key Laboratory of Environmental Biology and Pollution Control (Hunan University), Ministry of Education, Changsha, Hunan 410082, China

<sup>b</sup> Zhejiang Provincial Key Laboratory of Solid Waste Treatment and Recycling, College of Environmental Science and Engineering, Zhejiang Gongshang University, Hangzhou, Zhejiang 310018, China

## ARTICLE INFO

### Keywords:

MWCNTs  
Photocatalysis  
Catalyst  
Visible light  
Z-scheme mechanism

## ABSTRACT

Visible-light-driven photocatalysis as a promising technology has recently attracted great attention in environmental remediation. In this work, novel Z-scheme heterojunction photocatalysts Ag<sub>3</sub>PO<sub>4</sub>@MWCNTs@Cr:SrTiO<sub>3</sub> with excellent visible-light-driven photocatalytic performance and photostability were successfully synthesized and characterized. The photocatalytic activity for malachite green (MG) degradation was measured, and photodegradation mechanisms were investigated using GC–MS, ESR, and radical trapping experiments. On consideration of the practical applications, the effects of coexisting ions and pH were also evaluated. Results showed that significant changes of crystal size and micro-morphology for Ag<sub>3</sub>PO<sub>4</sub> were observed before and after the addition of MWCNTs, which transformed from a polyhedron with a diameter of about 30 μm into a spherical-like crystal with a diameter of 0.28–0.69 μm. This phenomenon was reported for the first time. The optimal catalyst with a dosage of 100 mg/g (the mass ratio of pollutant to photocatalyst) could reach 100% MG removal in 6 and 10 min under natural solar radiation and visible light irradiation, respectively. Results from the radical trapping experiments and ESR analysis confirmed that there existed the Z-scheme transfer mechanisms, and  $\cdot\text{O}_2^-$  and  $\text{h}^+$  played an important role during the photocatalytic degradation. Several small molecular organic acids such as acetic acid, glyoxylic acid, fumaric acid and benzoic acid were detected by GC–MS in the photodegradation products of MG, which further indicates that photocatalytic degradation pathway involved N-demethylation, benzene removal and open-ring reactions. The performance of the photocatalyst would be inhibited under strong acid condition or at the coexistence of certain concentration of  $\text{Cr}^{6+}$  and  $\text{Cl}^-$ . The novel addition of MWCNTs in the preparation and the changes of crystal structure and properties for the photocatalysts have the potential to promote the application of the photocatalysts for environmental remediation.

## 1. Introduction

Over the past decades, the increasingly severe energy crisis and environmental pollution have raised widespread concern, and the utilization of solar energy in environmental remediation has been paid close attention [1–3]. Semiconductor-based photocatalysis technique is such a promising and environmentally friendly technology [4,5]. Despite of its potential advantages, there are still challenges in this field such as maximizing the use of the solar energy, especially the visible-light energy [6]. TiO<sub>2</sub>, the most frequently used photocatalyst, can only

absorb the ultraviolet light energy that accounts for merely 4% of the sunlight energy, thus greatly impeding the use of the solar energy [7,8]. Therefore, investigations on developing efficient visible-light-driven photocatalysts have become a focus [9]. More recently, silver phosphate (Ag<sub>3</sub>PO<sub>4</sub>) stands out among numerous photocatalysts due to its excellent photocatalytic performance under visible-light irradiation, which can achieve quantum efficiencies of more than 90% ( $\lambda > 420 \text{ nm}$ ). Moreover, its high photooxidative capabilities for using dissolved oxygen in water and outstanding ability for degrading organic pollutants have been reported [10]. Unfortunately, the photocorrosion,

\* Corresponding authors at: College of Environmental Science and Engineering, Hunan University, Changsha, Hunan 410082, China.

E-mail addresses: [yangc@hnu.edu.cn](mailto:yangc@hnu.edu.cn), [yangcp@zjgsu.edu.cn](mailto:yangcp@zjgsu.edu.cn) (C. Yang), [LL0106@zjgsu.edu.cn](mailto:LL0106@zjgsu.edu.cn) (L. Lu).

<sup>1</sup> These authors contributed equally to this paper.

crystal size, and morphology of the photocatalyst hampered its photocatalytic activity and consequent practical applications. For example, Yang et al. found that  $\text{Ag}_3\text{PO}_4$  polyhedra with an average diameter of more than 15  $\mu\text{m}$  showed much less photocatalytic activity than sphere-like polyhedral morphology with an average diameter of 450 nm [11].

To overcome these problems, a lot of investigations have been performed, which mainly focus on improving synthesis procedures in controlling morphology and size and adding other materials to prepare silver phosphate-based heterostructured composite photocatalysts [10,12]. For instance, adding graphene to synthesize  $\text{Ag}_3\text{PO}_4$ -GR composites by hydrothermal approach has been reported as an effective way in control the morphology and size of  $\text{Ag}_3\text{PO}_4$  [12]. The formation of heterojunction is considered effective to inhibit the recombination of photogenerated electron-hole and to enhance photocatalytic activity. Several such heterostructured catalysts, including  $\text{Ag}_3\text{PO}_4/\text{TiO}_2$  [13],  $\text{AgX}/\text{Ag}_3\text{PO}_4$  ( $\text{X} = \text{Cl}, \text{Br}, \text{I}$ ) [14],  $\text{Ag}_3\text{PO}_4/\text{BiVO}_4$  [15],  $\text{Ag}_3\text{PO}_4/\text{graphene}$  [16] and  $\text{Ag}_3\text{PO}_4/\text{Ag}/\text{WO}_{3-x}$  [17] have been reported. Compared with above mentioned semiconductors,  $\text{SrTiO}_3$  is a stable semiconductor with the great potential in water splitting, and its minimum conduction band and maximum valence band are both negative compared to those of  $\text{Ag}_3\text{PO}_4$  [18]. Thus,  $\text{Ag}_3\text{PO}_4/\text{Cr-SrTiO}_3$  heterojunction photocatalyst, Cr-doped  $\text{SrTiO}_3$  with narrower band gap coupling with  $\text{Ag}_3\text{PO}_4$  could exhibit higher photodegradation efficiency for isopropyl alcohol [19]. Nevertheless, the photocatalytic activity of this binary system still needs improving. Furthermore, a more efficient Z-scheme heterojunction system has not been proposed and confirmed in this binary system, and low photocatalytic efficiency due to the size and morphology of  $\text{Ag}_3\text{PO}_4$  crystals could not be overcome neither.

Z-scheme system is inspired by photosynthesis of green plants which could turn water and  $\text{CO}_2$  into carbohydrates under visible light irradiation by two photoexcited process (photosystems I and II) [20,21]. Z-scheme heterojunction therefore means combining two different photocatalysts using an appropriate shuttle redox mediator to form two photochemical systems and an electron-transfer system, which could exhibit better performance in separating photogenerated electrons from holes and increasing their activity [22,23]. A Z-scheme photocatalytic system  $\text{BiVO}_4/\text{Au}/\text{CdS}$  showed better photocatalytic performance through the Z-scheme photocatalytic system than  $\text{BiVO}_4/\text{Au}$  and  $\text{BiVO}_4/\text{CdS}$  [24]. In this study,  $\text{Ag}_3\text{PO}_4$  and Cr-doped  $\text{SrTiO}_3$  are expected to be the photochemical system I (PS I) and PS II, respectively, and the small amount of Ag produced during the photocatalytic irradiation process as the electron-transfer system. This three-component system has the potential to construct the Z-scheme photocatalytic system. On this basis, considering the combination with other materials to further overcome the problems of photocorrosion, crystal size and morphology of  $\text{Ag}_3\text{PO}_4$ .

Multi-walled carbon nanotubes (MWCNTs) with unique electrical, optical and chemical properties show the potential to overcome these problems. MWCNTs was considered as one of the most promising carbon-based nanomaterial because of its outstanding properties, including i) high aspect ratio; ii) excellent electrical conductivity ( $> 10^5 \text{ S/m}$ ); iii) high Young's modulus ( $\approx 1 \text{ TPa}$ ); and iv) extraordinary tensile strength ( $\approx 60 \text{ GPa}$ ) [25–27]. Thus, MWCNTs could be an ideal additive to modify the properties of composites [28]. Most recently, a few research teams have combined MWCNTs with  $\text{Ag}_3\text{PO}_4$  to improve photocatalytic performance [29]. The photocatalyst of  $\text{Ag}_3\text{PO}_4\text{-WO}_3/\text{MWCNTs}$  were successfully prepared with high-performance for the simultaneous degradations of Cr(VI) and orange II [30]. The  $\text{AgBr-Ag}_3\text{PO}_4/\text{MWCNTs}$  composite fabricated via a chemical precipitation method shows excellent photocatalytic activity for the treatment of dye wastewater [31]. These successful cases demonstrated that MWCNTs could be the electron acceptor to increase the electron migration rate, improve the separation of carrier, and consequently enhance photocatalytic activity of the photocatalysts.

Unfortunately, data and reports on the investigations of sharp changes in size and morphology of  $\text{Ag}_3\text{PO}_4$  crystals caused by MWCNTs

have not been available. Additionally, the new photocatalyst which combines the advantages of Z-scheme heterojunction  $\text{Ag}_3\text{PO}_4/\text{Ag}/\text{Cr:SrTiO}_3$  and MWCNTs should have the potential of excellent visible-light-driven photocatalytic performance and photostability have not been reported. Therefore,  $\text{Ag}_3\text{PO}_4@\text{MWCNTs}/\text{Cr:SrTiO}_3$  was prepared and characterized in the present work, and its performance for MG degradation was evaluated. The mechanism about the notable change in the size and morphology of  $\text{Ag}_3\text{PO}_4$  crystals caused by the introduction of MWCNTs were discussed in detail. The photodegradation mechanisms were investigated using GC-MS, ESR, and radical trapping experiments.

## 2. Experimental

### 2.1. Material

Strontium acetate ( $\text{Sr}(\text{Ac})_2$ ) was purchased from Shanghai Mackin Biochemical Co. Ltd. Titanium isopropylate ( $[(\text{CH}_3)_2\text{CHO}]_4\text{Ti}$ ) was purchased from Shanghai Aladdin Biochemical Technology Co., Ltd. Multi-walled carbon nanotubes (MWCNTs) with nominal outer diameters of 10–20 nm were purchased from Nanjing Xianfeng Nano Materials Technology Co., Ltd. Disodium hydrogen phosphate dodecahydrate ( $\text{Na}_2\text{HPO}_4 \cdot 12\text{H}_2\text{O}$ ), silver nitrate ( $\text{AgNO}_3$ ), malachite green (MG) and other reagents were purchased from Sinopharm Chemical Reagent Co., Ltd (Shanghai, China). All the reagents and materials were of analytical grade, and de-ionized water ( $18.25 \text{ M}\Omega \cdot \text{cm}$ ) was used in the whole experiment.

### 2.2. Preparation of silver phosphate ( $\text{Ag}_3\text{PO}_4$ )

In a typical preparation procedure,  $\text{Na}_2\text{HPO}_4 \cdot 12\text{H}_2\text{O}$  aqueous solution (25 mL, 3 mmol) was added dropwise to the  $\text{AgNO}_3$  aqueous solution (25 mL, 9 mmol) with magnetically stirring in dark for 6 h. The golden precipitates were collected, washed by de-ionized water for several times, and finally dried in vacuum ( $55^\circ\text{C}$ ) overnight.

### 2.3. Preparation of $\text{Ag}_3\text{PO}_4@\text{MWCNTs}$

Firstly, 1.0 g of MWCNTs was placed in a flask containing 350 mL of  $\text{HNO}_3$  by magnetically stirring and refluxing at  $120^\circ\text{C}$  for 8 h. MWCNTs was separated by filtration, washed by de-ionized water until pH of 7, and finally dried at  $60^\circ\text{C}$  overnight. Secondly, a certain amount of MWCNTs was dispersed into de-ionized water via sonication for 3 h. Thirdly, 25 mL, 9 mmol  $\text{AgNO}_3$  aqueous solution was added to the above MWCNTs aqueous suspension and then stirred violently in dark for 12 h. And then  $\text{Na}_2\text{HPO}_4 \cdot 12\text{H}_2\text{O}$  aqueous solution (25 mL, 3 mmol) was added dropwise to the mixture with keeping stirring for 6 h in a dark condition. Finally, the obtained precipitate was washed with de-ionized water for several times, and dried in vacuum ( $55^\circ\text{C}$ ) overnight.

### 2.4. Preparation of Cr:SrTiO<sub>3</sub>

The synthetic method of Cr:SrTiO<sub>3</sub> was referred to previous reports [19,32]. Briefly, stoichiometric titanium isopropylate ( $[(\text{CH}_3)_2\text{CHO}]_4\text{Ti}$ ), Strontium acetate ( $\text{Sr}(\text{Ac})_2$ ), and  $\text{Cr}(\text{NO}_3)_3 \cdot 9\text{H}_2\text{O}$  were mixed thoroughly in dehydrated ethylene glycol with a molar ratio of 1:0.95:0.05. The mixed solution was heated at  $150^\circ\text{C}$  to evaporate the solvent completely, and the obtained grinding powders were added into NaOH aqueous solution (5 mol/L), and then the mixture was poured into the Teflon-lined stainless steel autoclave. This autoclave was heated up to  $180^\circ\text{C}$  and kept for 36 h. Finally, the obtained samples were processed by filtration, rinsed with ethanol and de-ionized water for several times, respectively, and dried in vacuum ( $55^\circ\text{C}$ ) overnight.

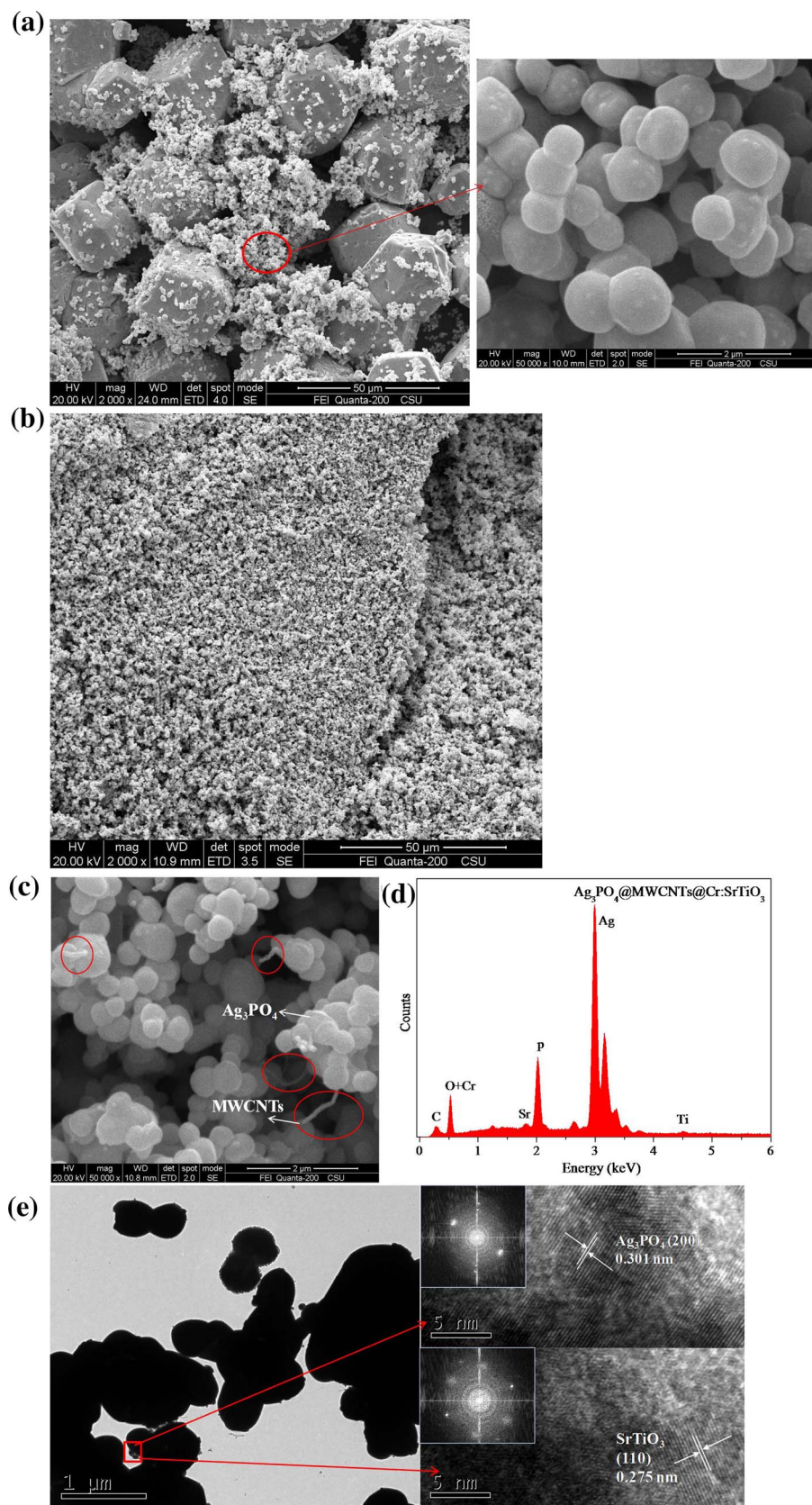


**Fig. 1.** SEM images of  $\text{Ag}_3\text{PO}_4$  (a) and  $\text{Ag}_3\text{PO}_4$ @MWCNTs composite (b,c); energy dispersive spectra (EDS) pattern of  $\text{Ag}_3\text{PO}_4$ @MWCNTs@Cr:SrTiO<sub>3</sub> composite (d). HRTEM images analysis of  $\text{Ag}_3\text{PO}_4$ @MWCNTs@Cr:SrTiO<sub>3</sub> composite (inset: FFT pattern) (e).

## 2.5. Preparation of $\text{Ag}_3\text{PO}_4$ @MWCNTs@ (7.5 wt%)Cr:SrTiO<sub>3</sub>

0.30 g  $\text{Ag}_3\text{PO}_4$ @MWCNTs were dispersed into de-ionized water and sonicated for 30 min, and then a certain amount polyvinyl pyrrolidone

(PVP) was added into the aqueous solution with magnetically stirring for 30 min. Then 0.0225 g Cr:SrTiO<sub>3</sub> was dispersed into de-ionized water and the solution was sonicated for 30 min. The Cr:SrTiO<sub>3</sub> aqueous solution was added dropwise into above solution with violent stirring.



After the mixture was stirred violently in dark for 4 h, the precipitate was collected and washed with de-ionized water and dried in vacuum (55 °C) overnight.

## 2.6. Characterization

The powder X-ray diffraction (XRD) patterns of as-prepared samples were carried out with Bruker AXS D8 advance diffractometer operating with Cu-K $\alpha$  radiation ( $\lambda = 0.15406$  nm) to investigate the crystal structure of the samples under 40 kV, 250 mA. The FTIR spectroscopy was measured with BRUKER fourier transform infrared spectrometer (VERTEX70) using the standard KBr disk method. The morphologies of samples were determined by scanning electron microscopy (SEM) (Quanta-200, FEI) and higher resolution transmission electron microscope (HRTEM) (TecnaiG2 F20, FEI). Chemical compositions of samples were analyzed using X-ray photoelectron spectroscopy (XPS, ESCALAB 250Xi, Thermo Fisher) and energy-dispersive X-ray spectroscopy (EDS). The photoluminescence (PL) spectra were studied through F-7000 fluorescence spectrometer. Ultraviolet visible diffuse reflectance spectra (UV-vis DRS) were recorded within the 300–800 nm wavelength range using UV-vis-NIR spectrophotometer (U-4100, Hitachi). Mott-Schottky plots were measured in 0.5 mol/L Na<sub>2</sub>SO<sub>4</sub> aqueous solution on a CHI 660C electrochemical analyzer (CHI Inc., USA), using a typical three-electrode system that consisted of a platinum wire counter electrode, a working electrode, and a saturated calomel reference electrode (SCE). The as-prepared photocatalysts thin film on fluorine-doped tin oxide (FTO) was used as the working electrode. The electron spin resonance (ESR) signals of radicals spin-trapped by spin-trapped reagent 5, 5-dimethyl-L-pyrroline N-oxide (DMPO) were examined on a JES FA200 electron paramagnetic resonance spectrometer under visible light irradiation ( $\lambda > 420$  nm).

## 2.7. Photocatalytic experiments

### 2.7.1. Degradation under artificial visible light irradiation

The photocatalytic activity of the obtained samples was evaluated by malachite green (MG) decomposition under visible light irradiation. A 300 W Xe lamp was employed as the light source with a 420 nm cut filter. In each experiment, 50 mg photocatalysts was dispersed in an aqueous solution of MG (200 mL, 25 mg/L). The mixed solution was stirred in dark for 30 min to reach the adsorption-desorption equilibrium before exposure to light. During the reaction, 3 mL of suspension was taken out at a given interval time, and then filtrated through a 0.22  $\mu$ m Millipore filter to remove the residual particles. The corresponding concentration of MG was monitored by a Shimadzu UV-vis spectrophotometer with the absorbance at the characteristic band of 617 nm. The degraded MG solution samples were determined by gas chromatography-mass spectrometry (GC-MS, Shimadzu). A Shimadzu QP-2010 GC-MS system was used for the analysis, which was equipped with a (30 m  $\times$  0.25 mm  $\times$  0.25  $\mu$ m) DB-5 ms column (Shimadzu) and used helium as carrier gas (1.0 mL/min).

### 2.7.2. Degradation under natural outdoor light

The procedure of MG degradation was also carried out under natural outdoor light irradiation, and the other conditions were the same as aforementioned.

## 3. Results and discussion

### 3.1. Characterization of the as-prepared samples

The morphology and microstructure of as-prepared samples were characterized by scanning electron microscopy (SEM). As presented in Fig. 1a, obviously, Ag<sub>3</sub>PO<sub>4</sub> polyhedra with an average diameter of about 30  $\mu$ m was observed, to which some small irregular sphere-like polyhedral particles were adhered, and they were Ag<sub>3</sub>PO<sub>4</sub> particles with

an average diameter of about 700 nm. Interestingly, after MWCNTs has been introduced into this system, large Ag<sub>3</sub>PO<sub>4</sub> particles with the diameter of 30  $\mu$ m no longer appeared (Fig. 1b). Instead, they all turn into smaller particles with the diameter of about 0.28–0.69  $\mu$ m, growing along the surface of MWCNTs (Fig. 1c). This might be attributed to electrostatic properties between the positive charged Ag<sup>+</sup> and the negative charged MWCNTs, which played an important role in the forming process of Ag<sub>3</sub>PO<sub>4</sub> seed particles and the growth pattern of Ag<sub>3</sub>PO<sub>4</sub> crystal particles [11]. In order to further determine the formation of the complex structure of Ag<sub>3</sub>PO<sub>4</sub>@MWCNTs@Cr:SrTiO<sub>3</sub>, a high-resolution transmission electron microscopy (HRTEM) image was provided, and the relative results were shown in Fig. 1e. It could be seen that the Cr:SrTiO<sub>3</sub> was attached to the Ag<sub>3</sub>PO<sub>4</sub> well. And the interplanar spacing of 0.301 nm was clearly observed, which corresponded to the (200) crystallographic planes of Ag<sub>3</sub>PO<sub>4</sub> (JCPDS no. 06-0505). Furthermore, the lattice fringe of 0.275 nm belonged to the (110) plane of SrTiO<sub>3</sub>, was in good agreement with the JCPDS card No. 35-0734, which provided evidence for the successful introduction of Cr:SrTiO<sub>3</sub> and the composite structure of Ag<sub>3</sub>PO<sub>4</sub>@MWCNTs@Cr:SrTiO<sub>3</sub>. Moreover, the EDS pattern also demonstrated that as-prepared composite was consisted of elemental Ag, P, O, C, Cr, Sr and Ti (Fig. 1d). The SEM pictures of the MWCNTs were also provided in Fig. S1. Notably, the SEM observations indicated that MWCNTs has significant influence on the morphology and size control of Ag<sub>3</sub>PO<sub>4</sub> particles, and the presence of MWCNTs was favorable for the formation of smaller Ag<sub>3</sub>PO<sub>4</sub> particles, which was beneficial for the photocatalytic performance.

The crystal structure properties of the prepared samples were evaluated by the X-ray diffraction (XRD) patterns, as shown in Fig. 2. It can be clearly seen that the diffraction peaks of Cr:SrTiO<sub>3</sub> could be in

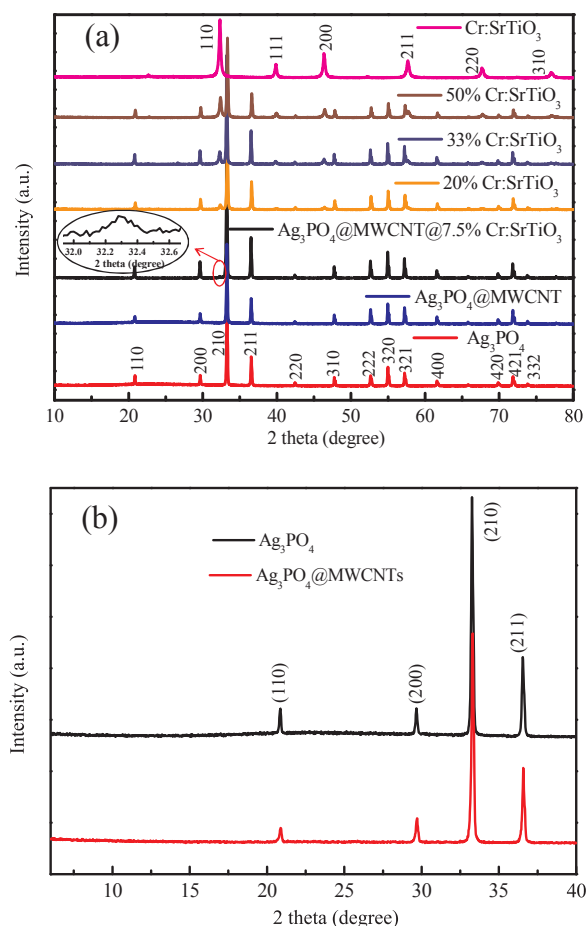


Fig. 2. XRD pattern of as-prepared samples.

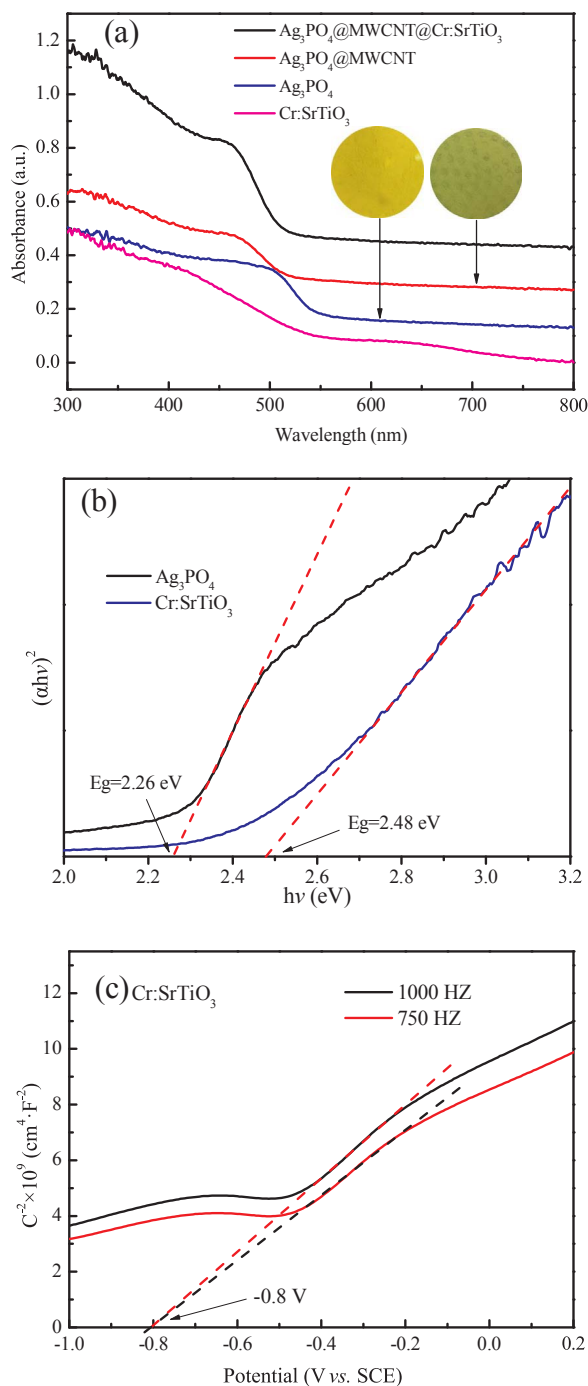


Fig. 3. (a) UV-vis diffuse reflectance spectra of different samples; (b) the band gap energy of different samples; (c) Mott-Schottky plots of Cr:SrTiO<sub>3</sub>.

good accordance with the perovskite structure with cubic symmetry of SrTiO<sub>3</sub>, which matched well with the standard XRD patterns (JCPDS no. 35-0734) [33]. Fig. 2a showed that positions of diffraction peaks of the Ag<sub>3</sub>PO<sub>4</sub> and Ag<sub>3</sub>PO<sub>4</sub>@MWCNTs samples were almost the same, both of which could be indexed to the body-centered cubic structure of Ag<sub>3</sub>PO<sub>4</sub> (JCPDS no. 06-0505). With the decrease of Cr:SrTiO<sub>3</sub> content in Ag<sub>3</sub>PO<sub>4</sub>@MWCNTs@Cr:SrTiO<sub>3</sub> composite, the intensity of Cr:SrTiO<sub>3</sub> peaks were decreased. The peaks belonged to Cr:SrTiO<sub>3</sub> in Ag<sub>3</sub>PO<sub>4</sub>@MWCNTs@7.5%Cr:SrTiO<sub>3</sub> could not be clearly observed due to the fairly low amount of Cr:SrTiO<sub>3</sub>. Under the state of amplification (Fig. 3a, inset), a characteristic peak at 2θ value of 32.32° could be attributed to the (110) crystal plane of SrTiO<sub>3</sub>. Besides, evident changes in the intensity ratios for various peaks of Ag<sub>3</sub>PO<sub>4</sub> were observed

following the introduction of MWCNTs (Fig. 3b). The (110) and (200) peaks were 0.99 and 0.64 for the Ag<sub>3</sub>PO<sub>4</sub> and Ag<sub>3</sub>PO<sub>4</sub>@MWCNTs, respectively, which decreased by 35%. According to the findings in previous studies [10], the intensity ratio for the (110) and (200) peaks for the Ag<sub>3</sub>PO<sub>4</sub> rhombic dodecahedrons was remarkably higher than Ag<sub>3</sub>PO<sub>4</sub> cubes, which implied that the introduction of MWCNTs might have changed the crystal structure of Ag<sub>3</sub>PO<sub>4</sub>. The results of XRD were well in agreement with the findings of the SEM and further validated the influence of MWCNTs, and implied the well connection among the Ag<sub>3</sub>PO<sub>4</sub>, Cr:SrTiO<sub>3</sub> and MWCNTs was built.

UV-vis diffuse reflectance spectrum (DRS) was measured to evaluate the optical properties of as-prepared samples, and the results were shown in Fig. 3a. The DRS absorption spectra revealed that Ag<sub>3</sub>PO<sub>4</sub> and Ag<sub>3</sub>PO<sub>4</sub>@MWCNTs both exhibited excellent absorption at the wavelength of less than 500 nm. While compared with the Ag<sub>3</sub>PO<sub>4</sub>, there was an obviously enhanced absorbance for Ag<sub>3</sub>PO<sub>4</sub>@MWCNTs, which implied that the MWCNTs was successfully incorporated into Ag<sub>3</sub>PO<sub>4</sub> and contributed to promoting the optical absorption capacity. Moreover, it was observed that the colors changed from golden yellow to olive, corresponding to Ag<sub>3</sub>PO<sub>4</sub> and Ag<sub>3</sub>PO<sub>4</sub>@MWCNTs, respectively. Specially, Ag<sub>3</sub>PO<sub>4</sub>@MWCNTs@Cr:SrTiO<sub>3</sub> showed the most intense absorption in the region from 300 to 800 nm, indicating the distinctly enhanced adsorption following the introduction of Cr:SrTiO<sub>3</sub>. The good results might be attributed to the forming of ternary heterojunction composites that owned reasonable structure configuration and suitable band matching. The bandgap edge (E<sub>g</sub>) of a semiconductor can evaluate the production and transformation of electron-hole pairs, and the E<sub>g</sub> values of as-prepared samples were calculated by the Kubelka-Munk equation [34]:

$$(\alpha h\nu)^n = A(h\nu - E_g) \quad (1)$$

Where  $\alpha$ ,  $h$ ,  $\nu$ ,  $A$  and  $E_g$  are absorption coefficient, Planck constant, light frequency, proportionality constant, and optical band gap energy, respectively. And  $n$  value is determined by the type of optical transition of semiconductors ( $n = 2$  for direct transition and  $n = 1/2$  for indirect transition) [35]. Both Ag<sub>3</sub>PO<sub>4</sub> and Cr:SrTiO<sub>3</sub> belong to the indirect transition semiconductors. According to the results in Fig. 3b, E<sub>g</sub> values of the samples were estimated to be 2.26 eV and 2.48 eV, corresponding to Ag<sub>3</sub>PO<sub>4</sub> and Cr:SrTiO<sub>3</sub> composite, respectively. Moreover, Mott-Schottky plot was used to characterize the flat band potential, and the values were determined using the Mott-Schottky equation [36]:

$$\frac{1}{C_{sc}^2} = \frac{2}{e\epsilon\epsilon_0 N} \left( E - E_{fb} - \frac{KT}{e} \right) \quad (2)$$

Where  $C_{sc}$  is the capacitance of the space charge region,  $\epsilon$  is the dielectric constant of the semiconductor,  $\epsilon_0$  is the permittivity of free space,  $N$  is the donor density,  $k$  is Boltzmann's constant,  $T$  is the temperature,  $q$  is the electronic charge,  $E$  and  $E_{fb}$  is the applied potential and flatband potential, respectively. So the  $E_{fb}$  value can be determined from the extrapolation to  $1/C^2 = 0$ . As shown in Fig. 3c,  $E$  value was estimated to be  $-0.8$  V. As the value of  $KT/e = 0.0257$ , so the flat potential was calculated to be  $-0.83$  V versus the saturated calomel electrode (SCE), which was equivalent to  $-0.59$  V versus the normal hydrogen electrode (NHE). The conduction band potential ( $E_{CB}$ ) of  $n$ -type semiconductors is about 0.2 eV higher than the flat potentials ( $E_{CB} \approx E_{fb} + 0.2$ ) [37]. So the  $E_{CB}$  value and corresponding valence band potential ( $E_{VB}$ ) of Cr:SrTiO<sub>3</sub> were calculated to be  $-0.79$  eV and  $1.69$  eV. The Ag<sub>3</sub>PO<sub>4</sub> thin film on fluorine-doped tin oxide (FTO) was also used as the working electrode, and the electrochemical flat potential measurements were carried out. However, the yellow working electrode was converted into other black material during the test, which may ascribe to the instability of the Ag<sub>3</sub>PO<sub>4</sub>. Therefore, this method is not suitable for the determination of Ag<sub>3</sub>PO<sub>4</sub> conduction band potential. Instead, the  $E_{CB}$  and  $E_{VB}$  of Ag<sub>3</sub>PO<sub>4</sub> were obtained by theoretical calculation, and the equations were as following [38]:

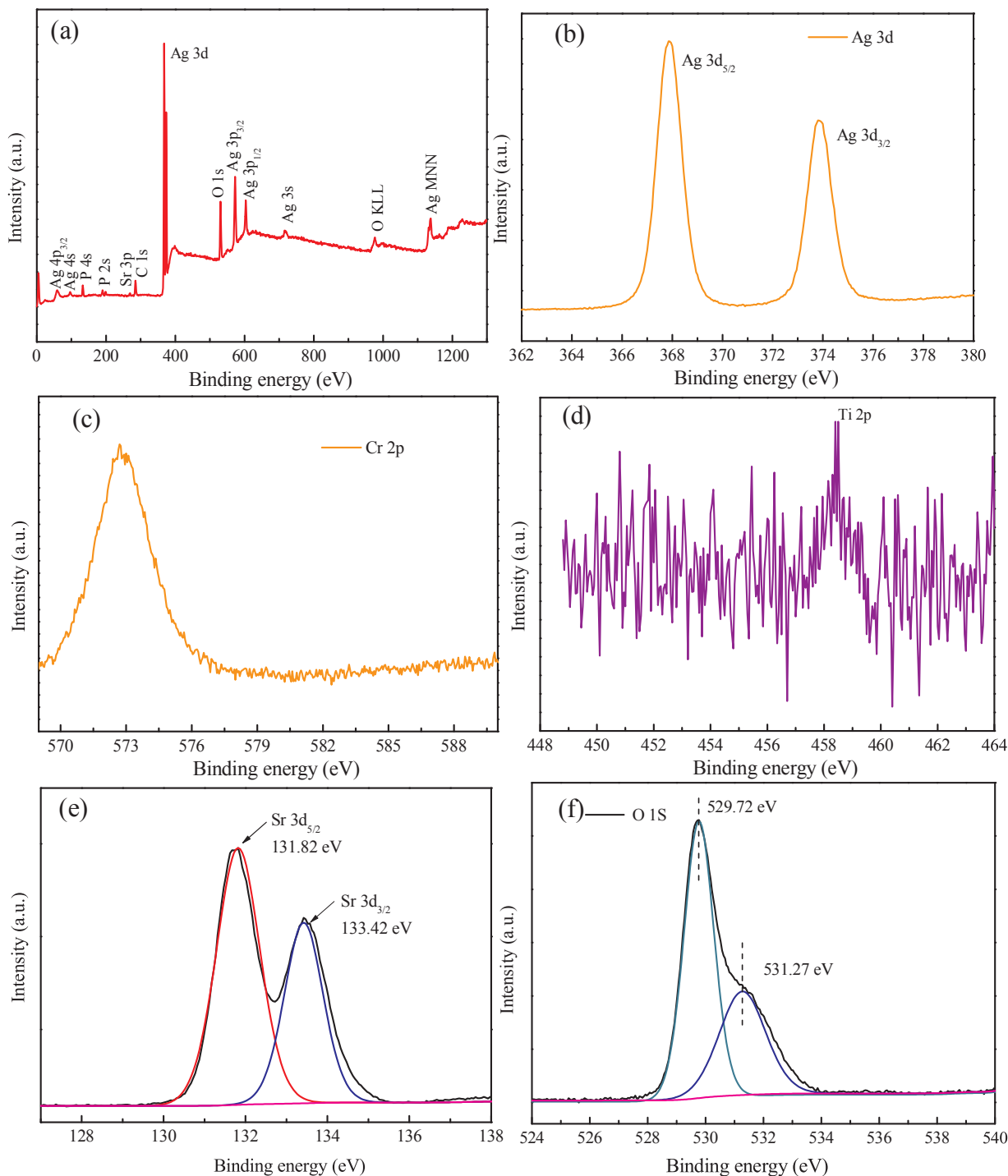


Fig. 4. (a) XPS survey spectra; high resolution XPS spectrum of (b) Ag 3d, (c) Cr 2p and (d) Ti 2p.

$$E_{CB} = X - E_C - 1/2E_g \quad (3)$$

$$E_{VB} = E_{CB} + E_g \quad (4)$$

Where,  $X$  is the electronegativity of the semiconductor calculated by geometric mean of the Pearson absolute electronegativity, so the value of  $X$  for  $Ag_3PO_4$  is 5.96 eV.  $E_C$  is the energy of free electrons on the hydrogen scale (about 4.50 eV vs NHE). Therefore, the  $E_{CB}$  potentials of  $Ag_3PO_4$  were +0.33 eV, and corresponding  $E_{VB}$  potentials could calculate to be +2.59 eV. The calculated values were in good agreement with the previous report [39,40].

The surface chemical composition and electronic state of  $Ag_3PO_4@MWCNTs@Cr:SrTiO_3$  composite were determined by the X-ray

photoelectron spectroscopy (XPS). It was obviously seen that all elements of Ag, P, O, C and Sr except Cr and Ti could be found in the XPS survey spectrum (Fig. 4a). In order to further prove the existence of Cr and Ti and investigate their chemical states, high-resolution XPS spectra of Cr 2p and Ti 2p (Fig. 4c and d) were provided. And the typical peaks were located at 572.7 eV and 458.5 eV, which could ascribe to binding energies of Cr 2p and Ti 2p, respectively. As shown in Fig. 4b, the Ag 3d<sub>5/2</sub> and 3d<sub>3/2</sub> peaks were observed at 367.9 eV and 373.8 eV, respectively, which indicated the existence of Ag<sup>+</sup>. And no other XPS peak corresponding to silver (580.2 eV) was observed. Two main peaks (Fig. 4e) appearing at the binding energies of 131.82 eV and 133.42 eV belonged to Sr 3d<sub>5/2</sub> and Sr 3d<sub>3/2</sub>, respectively. As shown in

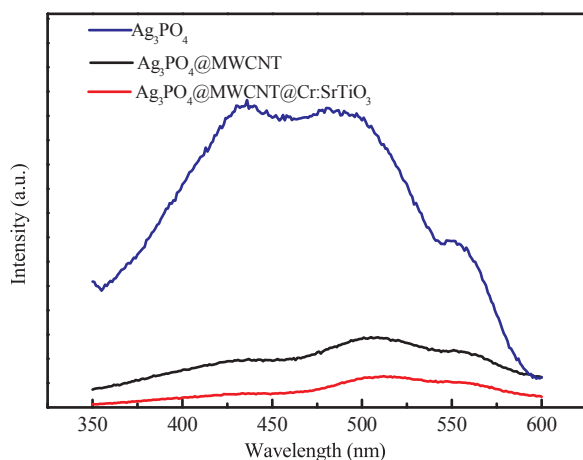


Fig. 5. Photoluminescence (PL) spectra of the prepared samples.

Fig. 4f, the O 1s peaks could be divided into two different peaks at 531.27 eV and 529.72 eV, respectively. These were in agreement with  $O^{2-}$  anion from the  $Ag_3PO_4$  and the hydroxyl group [41]. The results of XPS were consistent with that of EDS. And the FTIR spectra of different samples were provided in Fig. 2S. Based on the results of SEM, HRTEM, XRD, DRS, EDS, FTIR and XPS measurements, the close combination among  $Ag_3PO_4$ , MWCNTs and Cr:SrTiO<sub>3</sub> in  $Ag_3PO_4$ @MWCNTs@Cr:SrTiO<sub>3</sub> system had been fully validated.

In order to study the separation and recombination and investigate the rate of photoproduced electron-hole pairs in semiconductors, a photoluminescence (PL) spectroscopy study was performed. The PL spectrum intensity is dependent on the number of electron-hole recombination. Hence the high PL spectrum intensity means high photoproduced electron-hole pairs recombination rate and poor photocatalytic activity [42]. Fig. 5 presented the PL spectra of samples at an excitation wavelength of 320 nm. Obviously,  $Ag_3PO_4$  showed the highest PL peak intensity, which revealed the easy recombination of photoproduced electron-hole pairs. However, after the MWCNTs coupled, the formed  $Ag_3PO_4$ @MWCNTs presented a much lower PL peak intensity than  $Ag_3PO_4$ . These results indicated that the recombination of the photoproduced electrons and holes was inhibited effectively, which might result from that the MWCNTs can act as the capture trap of the photoproduced carriers, increasing the photoproduced charge diffusion rate and charge mobility effectively. Additionally, the lowest charge recombination efficiency of  $Ag_3PO_4$ @MWCNTs@Cr:SrTiO<sub>3</sub> was observed, implying that an effective heterojunction was fabricated successfully, which can further depress the recombination of photo-generated electron-hole pairs and prolong carrier lifetime.

### 3.2. Photocatalytic performance under artificial visible light and sunlight irradiation

Malachite green (MG), one kind of biocide, food additive and coloring agent, was chosen as an organic pollutant to evaluate the photocatalytic activities of the as-prepared photocatalysts. In each experiment, 50 mg photocatalyst was dispersed in an aqueous solution of MG (25 mg/L, 200 mL), then the mixed solution was stirred in dark for 30 min to reach the adsorption-desorption equilibrium. And finally, 300 W Xe lamp ( $\lambda > 420$  nm) was employed as the artificial light source to carry out the photodegradation experiment. As shown in Fig. 6a, all the MWCNTs@ $Ag_3PO_4$  hybrids exhibited higher photocatalytic activities than pure  $Ag_3PO_4$ . Especially, under the visible light irradiation for 12 min, 100% of MG had been degraded by the MWCNTs@ $Ag_3PO_4$  composite with the loading ratios of MWCNTs for 0.5%, 0.75% and 1.0%. By comparison, 0.75%MWCNT@ $Ag_3PO_4$  exhibited the highest photocatalytic activity. However, after 30 min of exposure to visible light, the  $Ag_3PO_4$  only gave the degradation of 99%,

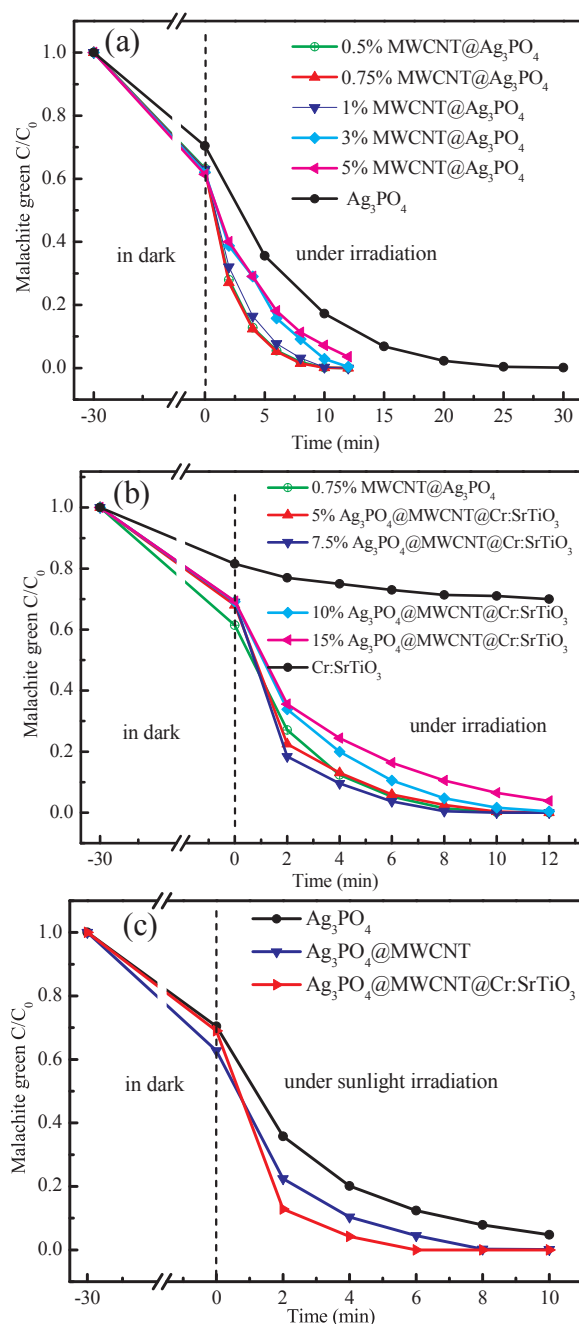


Fig. 6. Photodegradation curves of MG in the presence of as-prepared samples with different loading ratios of (a) MWCNTs and (b) Cr:SrTiO<sub>3</sub>; (c) photodegradation curves of MG under the natural sunlight irradiation with different samples.

which suggested that the combination of  $Ag_3PO_4$  with MWCNTs is an effective way to improve the photocatalytic activity. Comparing with  $Ag_3PO_4$ , Cr:SrTiO<sub>3</sub> and  $Ag_3PO_4$ @MWCNTs composite, the ternary 7.5%-Cr:SrTiO<sub>3</sub>@MWCNTs@ $Ag_3PO_4$  composite exhibited the highest photocatalytic activity and 100% of MG was removed at a faster rate under irradiation for 10 min (Fig. 6b). Moreover, to further prove that MG had been completely photodegraded, absorption spectra of MG solutions in the presence of 7.5%-Cr:SrTiO<sub>3</sub>@MWCNTs@ $Ag_3PO_4$  with different irradiation time was provided (Fig. S3). The result showed that the typical peak of MG at 617 nm and the absorbance decreased to zero during the photodegradation. The better photocatalytic properties and faster reaction rate of the ternary composite should be attributed to the coexisting effects among  $Ag_3PO_4$ , MWCNTs and Cr:SrTiO<sub>3</sub>, which could elevate the photoproduced electron-hole pairs separation by the



formation of strong interfacial interaction via heterojunction among different components. Furthermore, considering the practical application value of the photocatalysts, the degradation performance of MG solution under natural sunlight irradiation was also investigated (Location: Hunan University, N28°10'54" E112°56'18"; Date: May 27, 2017; Weather: Clear day). And the solar intensity measured by light meter was presented in Table S1. Surprisingly, as shown in Fig. 6c, all the prepared photocatalysts exhibited better photocatalytic activity under sunlight irradiation, suggesting that as-prepared composite catalyst, as an innovative full-spectrum photocatalyst, could effectively utilize natural sunlight in environmental remediation process. Especially, with the dosage of 100 mg/g (the mass ratio of pollutant to photocatalyst), the synthesized ternary composite achieved the highest photocatalytic performance, merely taking about 6 min to degrade MG completely. In view of the excellent performance of  $\text{Ag}_3\text{PO}_4@\text{MWCNTs@Cr:SrTiO}_3$  composite, it could be regarded as a promising, green and effective photocatalyst and applied to environmental treatment.

### 3.3. Effects of coexisting inorganic salts and the pH value

In practical wastewater systems, pH values and coexisting inorganic salts might be the major factors deteriorating dye wastewater disposal. Herein, a series of experiments under different pH values and inorganic salts were conducted. The effects of different inorganic salts were shown in Fig. 7a, and all kinds of ion concentrations were provided in Table S2. Obviously, no apparent differences appeared in the degradation curves of the solutions containing  $\text{K}_2\text{SO}_4$  and  $\text{NaNO}_3$ , which indicated that  $\text{K}^+$ ,  $\text{SO}_4^{2-}$ ,  $\text{Na}^+$  and  $\text{NO}_3^-$  do not affect the degrading performance of  $\text{Ag}_3\text{PO}_4@\text{MWCNTs@Cr:SrTiO}_3$  composite. However,

the negative effect was found in the presence of  $\text{K}_2\text{Cr}_2\text{O}_7$ , and the decrease in the photodegradation of MG might be ascribed to the competitive adsorption between  $\text{Cr}_2\text{O}_7^{2-}$  and MG on the surface of the catalyst that caused the reduction of active site [43]. Interestingly, when KCl was added into MG solution, high removal rate of MG was obtained immediately after ultrasonic dispersion (about 2 min), but remained approximately constant when it under irradiation. According to previous reports, flux of cations in dyes determines the decoloration rate. And Liu et al. also found that under similar conditions, the degradation ratio for MG in the presence of KCl is 100.0%, while it was only 29.0% and 61% in the presence of NaCl and  $\text{KNO}_3$ , respectively [44]. Hence the rapidly removal of MG in a short time may result from the change in properties of MG caused by interaction among  $\text{K}^+$ ,  $\text{Cl}^-$  and MG. As for the subsequent inhibition, the phenomenon might be attributed to the following two reasons. First,  $\text{Ag}_3\text{PO}_4$  may be converted to AgCl partially during photodegradation [43]. Second, chloride anions are the scavenger of the hydroxyl radicals, which would also led to the decline of sample performance [44]. The effect of pH values on the MG degradation was presented in Fig. 7b, when the pH values were within the range of 5–9, high degradation efficiency of MG were all obtained, which indicated that the  $\text{Ag}_3\text{PO}_4@\text{MWCNTs@Cr:SrTiO}_3$  composite could be applied to relatively wide range of pH. As for the highest removal efficiency at the pH values of 11.01, the fading of MG under strong alkali condition was presumably responsible [45]. Moreover, the initial pH of the aqueous solution might have a great effect on the adsorption behavior of pollutants and the generation of ROSs during the process of photocatalytic reaction [45,46]. When the pH value was too low, it may cause the changing of Zeta potentials of photocatalysts, decreasing the forming of hydroxyl radicals. Hence, an unsatisfactory photocatalytic activity at the pH values of 2.98 may result from the presence of  $\text{H}^+$  ions competing with MG molecules for adsorption sites of photocatalyst and the reduction of hydroxyl radicals. In summary, the proper concentrations of  $\text{K}^+$ ,  $\text{SO}_4^{2-}$ ,  $\text{Na}^+$  and  $\text{NO}_3^-$ , and appropriate pH range of solution do not affect the catalysis activities of  $\text{Ag}_3\text{PO}_4@\text{MWCNTs@Cr:SrTiO}_3$  composite. However, the performance of photocatalyst and the photodegradation process would be suppressed under the influence of extreme pH values (such as pH = 3, 11) or the coexistence of certain concentration  $\text{Cr}^{6+}$  and  $\text{Cl}^-$ . The results suggested that, except for extreme conditions, as-prepared samples could serve as an efficient photocatalyst in practical application.

### 3.4. Photostability and recyclability

The repeatability and stability of the photocatalysts are significant factors in their practical application. So the photocatalytic repeatability of the as-prepared samples was studied by recycling experiment, and the results were shown in Fig. 8a. It could be clearly seen that the photocatalytic activity of the  $\text{Ag}_3\text{PO}_4@\text{MWCNTs@Cr:SrTiO}_3$  composite had no apparent deactivation even after five successive recycles for the decomposition of MG under visible light irradiation. Moreover, it could be observed that the photocatalytic activity of  $\text{Ag}_3\text{PO}_4@\text{MWCNTs}$  catalyst was also barely declined, while the degradation efficiency for pure  $\text{Ag}_3\text{PO}_4$  had a significant loss, which indicated that the introduction of MWCNTs could improve the photostability of  $\text{Ag}_3\text{PO}_4$ . The remarkable decrease for the photocatalytic performance of  $\text{Ag}_3\text{PO}_4$  might be due to the partial reduction of  $\text{Ag}_3\text{PO}_4$  into  $\text{Ag}^0$  by photoproduced electrons. However, the presence of conductive MWCNTs can serve as an effective acceptor of the photoproduced electrons, hence, the photogenerated CB electrons of  $\text{Ag}_3\text{PO}_4$  can be transferred to MWCNTs in the  $\text{Ag}_3\text{PO}_4@\text{MWCNTs}$  or the  $\text{Ag}_3\text{PO}_4@\text{MWCNTs@Cr:SrTiO}_3$  composite. In this way, it can suppress the charge recombination and reduce the decomposition rates of  $\text{Ag}^+$  to metallic Ag effectively in the photocatalytic process, and finally improve the photocatalytic activity and repeatability of the photocatalysts. To further demonstrated the stability of the  $\text{Ag}_3\text{PO}_4@\text{MWCNTs@Cr:SrTiO}_3$  composite, the XRD of the fresh and used photocatalyst have been provided for comparison (Fig. 8b). The results

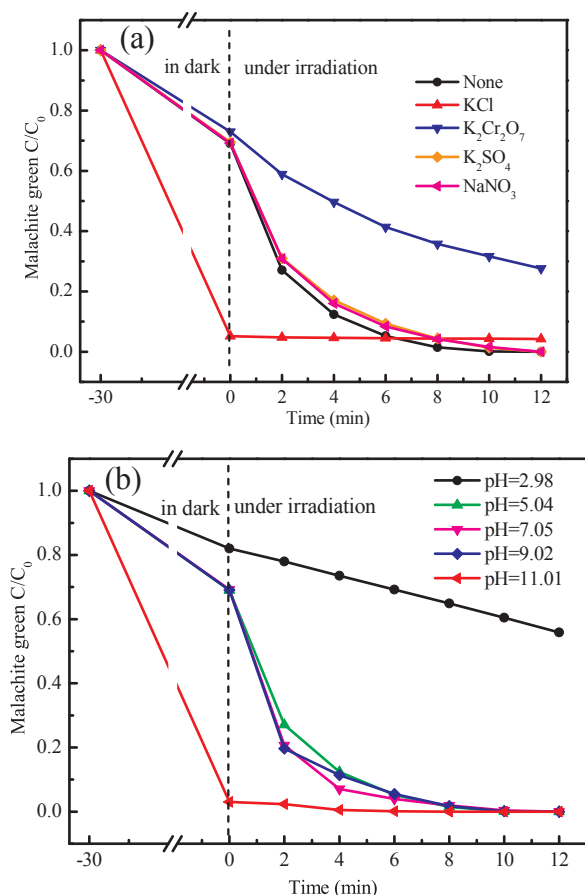


Fig. 7. Photodegradation curves of MG solution containing different inorganic salts (a) and at different pH condition (b).



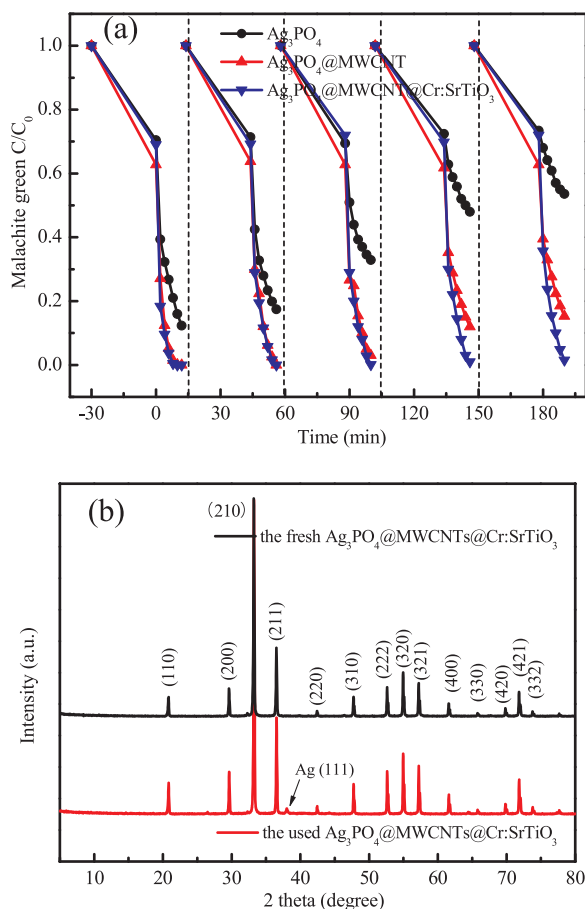


Fig. 8. Cycling runs for the photocatalytic degradation of MG in the presence of different as-prepared samples; (b) XRD patterns of the fresh and used  $\text{Ag}_3\text{PO}_4@\text{MWCNTs}@\text{Cr:SrTiO}_3$  composite.

revealed that no significant changes happened in the crystal structure and the weak characteristic peak at  $2\theta$  value of  $38.04^\circ$  could be attributed to the (111) crystal plane of metallic Ag. According to previous reports, the existence of minor amount of Ag will not reduce the photocatalytic efficiency, but instead it may play an important role in forming Z-scheme heterojunction with superior photoactivity enhancement [17,47–49]. The results of this study also have proved this point, and the mechanism would be explained in detail in the mechanism section.

### 3.5. Possible photocatalytic mechanism of $\text{Ag}_3\text{PO}_4@\text{MWCNTs}@\text{Cr:SrTiO}_3$

In order to investigate possible photocatalytic mechanism of  $\text{Ag}_3\text{PO}_4@\text{MWCNTs}@\text{Cr:SrTiO}_3$  composite, radical trapping experiment of different active species had been carried out to explore the predominant active species generated in the reaction system. The benzoquinone (BQ), ethylenediamine tetra acetic acid disodium salt (EDTA-2Na), isopropanol (IPA) and  $\text{AgNO}_3$  were employed as the scavengers of superoxide radical ( $\cdot\text{O}_2^-$ ), hole ( $\text{h}^+$ ), hydroxyl radical ( $\cdot\text{OH}$ ) and photogenerated electron ( $\text{e}^-$ ), respectively. The dosages of all sacrificial agents were provided in Table S3. As depicted in Fig. 9, the addition of IPA had little effect on photodegradation performance of MG, indicating that few  $\cdot\text{OH}$  was involved in the photocatalytic processes. However, the presence of BQ,  $\text{AgNO}_3$  and EDTA-2Na brought about marked deactivation of the  $\text{Ag}_3\text{PO}_4@\text{MWCNTs}@\text{Cr:SrTiO}_3$  photocatalyst and the photodegradation performance was sharply decreased. The results suggested that  $\cdot\text{O}_2^-$  and  $\text{h}^+$  played an important role in the degradation of MG. To further identify the radical generation in this photocatalytic system under visible irradiation ( $\lambda > 420 \text{ nm}$ ), the ESR

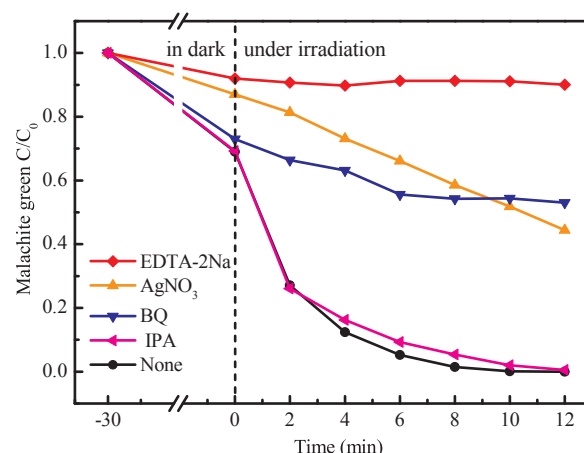
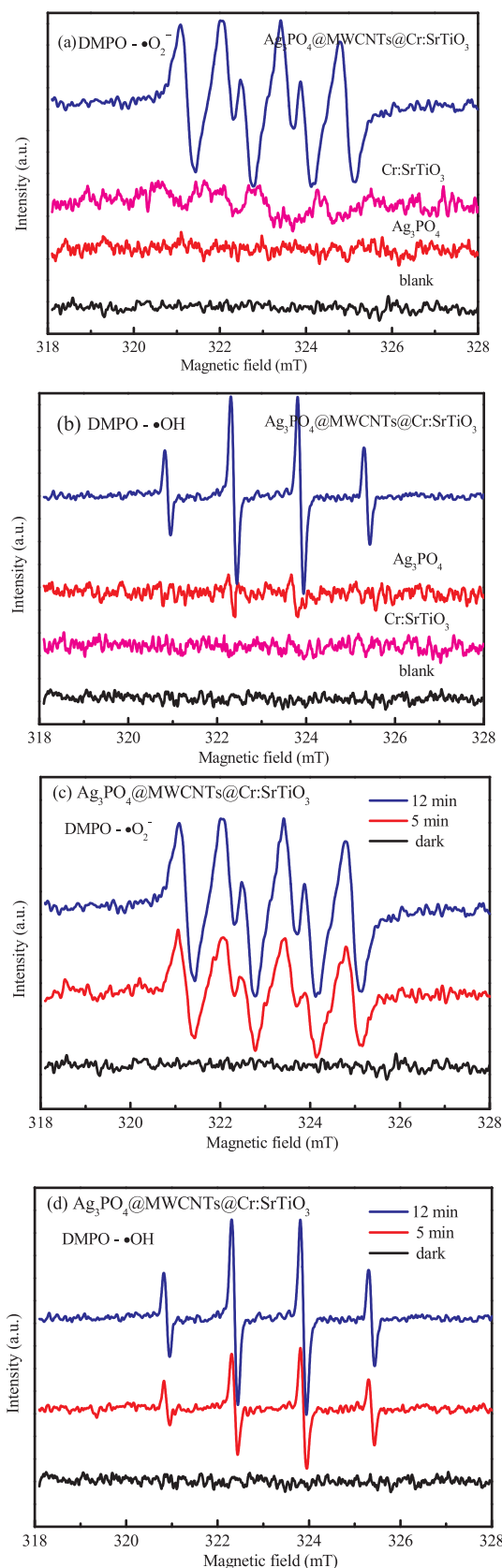


Fig. 9. Photodegradation curves of MG over  $\text{Ag}_3\text{PO}_4@\text{MWCNTs}@\text{Cr:SrTiO}_3$  composite with different active species scavengers under visible light irradiation.

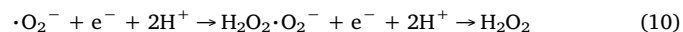
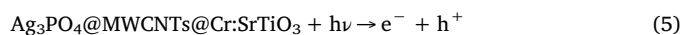
spin-trap with DMPO technique was performed on illuminated  $\text{Ag}_3\text{PO}_4$ ,  $\text{Cr:SrTiO}_3$  and  $\text{Ag}_3\text{PO}_4@\text{MWCNTs}@\text{Cr:SrTiO}_3$  respectively. And the experiments were carried out under dark condition and visible light irradiation for 12 min, respectively. As shown in Fig. 10a, there was no  $\text{DMPO} \cdot \text{O}_2^-$  signal when illuminating  $\text{Ag}_3\text{PO}_4$ , which suggested that the single  $\text{Ag}_3\text{PO}_4$  cannot produce  $\cdot\text{O}_2^-$ . Several weak signal peaks could be observed in  $\text{Cr:SrTiO}_3$ -DMPO system when exposed to visible light, implying that the single  $\text{Cr:SrTiO}_3$  had the ability to produce  $\cdot\text{O}_2^-$ . And the appearance of the weak signal might be ascribed to the fast recombination rate of photogenerated electron-hole pairs in single  $\text{Cr:SrTiO}_3$ . However, distinct characteristic peaks of  $\cdot\text{O}_2^-$  signals could be clearly detected in  $\text{Ag}_3\text{PO}_4@\text{MWCNTs}@\text{Cr:SrTiO}_3$  composite. Besides, the signal of  $\cdot\text{OH}$  was also detected in DMPO system and the results were provided in Fig. 10b. Similarly,  $\cdot\text{OH}$  signals were obviously observed in the  $\text{Ag}_3\text{PO}_4@\text{MWCNTs}@\text{Cr:SrTiO}_3$  composite. While there was several weak signals in the single  $\text{Ag}_3\text{PO}_4$  system and almost no signal with single  $\text{Cr:SrTiO}_3$ , which also suggested that the single  $\text{Cr:SrTiO}_3$  cannot produce  $\cdot\text{OH}$ . Moreover, the ESR test was also carried out on illuminated  $\text{Ag}_3\text{PO}_4@\text{MWCNTs}@\text{Cr:SrTiO}_3$  composite under dark condition and visible light irradiation for 5 min and 12 min. As shown in Fig. 10c, some obvious characteristic peaks of  $\text{DMPO} \cdot \text{O}_2^-$  were observed in methanol dispersion under visible light irradiation and gradually increasing signal intensity can be seen apparently. While there was no signal found in dark condition. Similarly, gradually increasing intensity of  $\text{DMPO} \cdot \text{OH}$  signals were also detected successfully in aqueous dispersion (Fig. 10d). The ESR results suggested that  $\cdot\text{O}_2^-$  and  $\cdot\text{OH}$  radicals could be produced successfully on the surface of visible light-irradiated  $\text{Ag}_3\text{PO}_4@\text{MWCNTs}@\text{Cr:SrTiO}_3$  composite, which were consistent with the results of radical trapping experiments. And this provided further evidences to prove that  $\cdot\text{O}_2^-$  and  $\cdot\text{OH}$  radicals were produced by  $\text{Ag}_3\text{PO}_4@\text{MWCNTs}@\text{Cr:SrTiO}_3$  composite rather than the single  $\text{Cr:SrTiO}_3$  or  $\text{Ag}_3\text{PO}_4$ .

On the basis of the above experimental data and theoretical analysis, a reasonable photocatalytic mechanism promoting degradation of MG by  $\text{Ag}_3\text{PO}_4@\text{MWCNTs}@\text{Cr:SrTiO}_3$  composite was proposed, as represented in Fig. 11. According to the calculation results above, the optical band gap of  $\text{Ag}_3\text{PO}_4$  and  $\text{Cr:SrTiO}_3$  are 2.26 eV and 2.48 eV, respectively. The CB and VB edge potentials of  $\text{Ag}_3\text{PO}_4$  are at +0.33 eV and +2.59 eV, and the corresponding CB and VB edge potentials of  $\text{Cr:SrTiO}_3$  are at -0.79 eV and +1.69 eV, respectively. Hence, under visible light irradiation, the electrons at the valence band (VB) of  $\text{Ag}_3\text{PO}_4$  and  $\text{Cr:SrTiO}_3$  both could easily be excited to the conduction band (CB), inducing the formation of holes in the VB. According to the previous reports, the separation of photogenerated electron-hole pairs could be interpreted by general heterostructured mechanism [19]. As shown in Fig. 11a, photogenerated electrons in the CB of  $\text{Cr:SrTiO}_3$



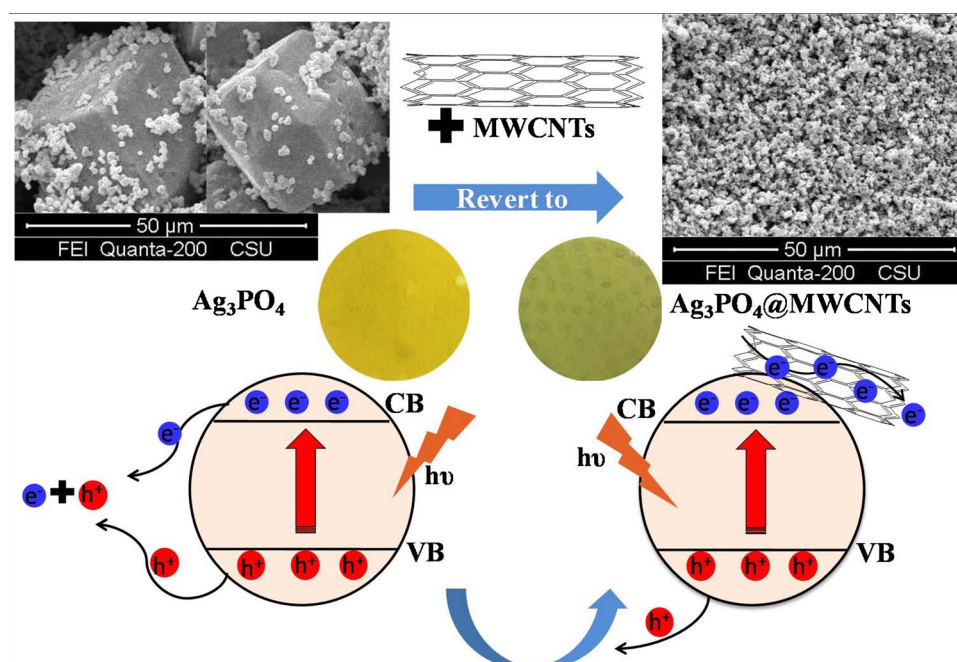
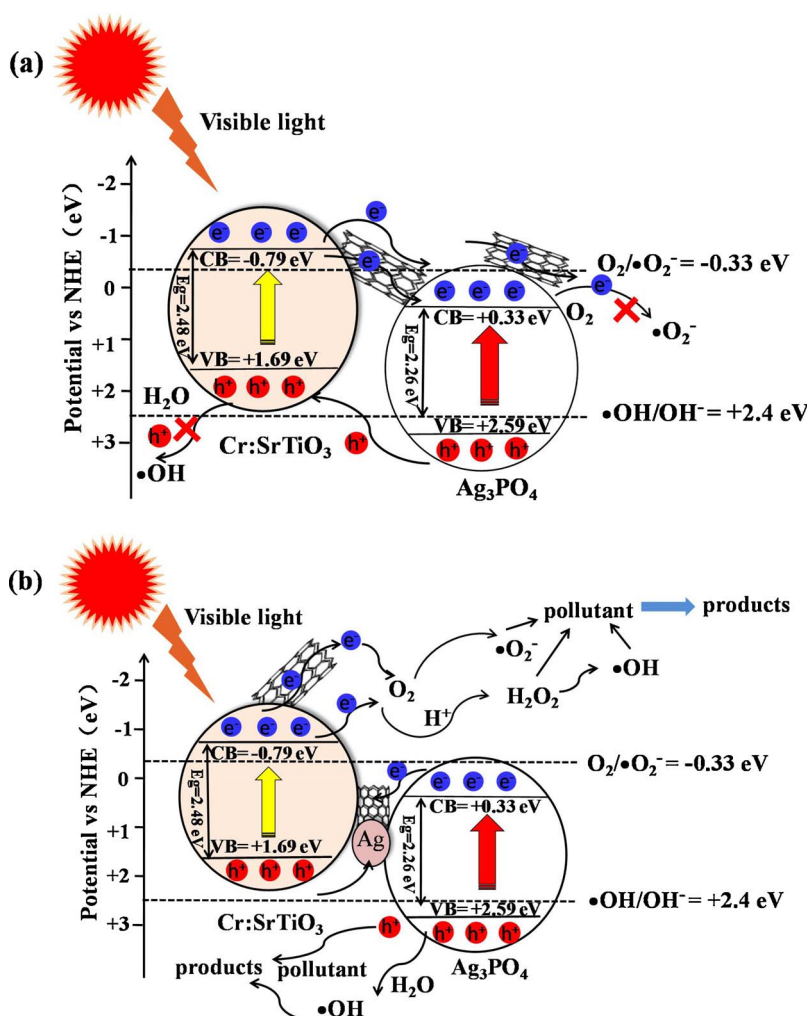
**Fig. 10.** ESR spectra of radical adducts trapped by DMPO in the  $\text{Ag}_3\text{PO}_4$ @MWCNTs@Cr:SrTiO<sub>3</sub>,  $\text{Ag}_3\text{PO}_4$  and Cr:SrTiO<sub>3</sub> dispersion under both the dark and visible light irradiation ( $\lambda > 420$  nm) condition: (a,c) in methanol dispersion for DMPO- $\cdot\text{O}_2^-$ ; (b,d) in aqueous dispersion for DMPO- $\cdot\text{OH}$ .

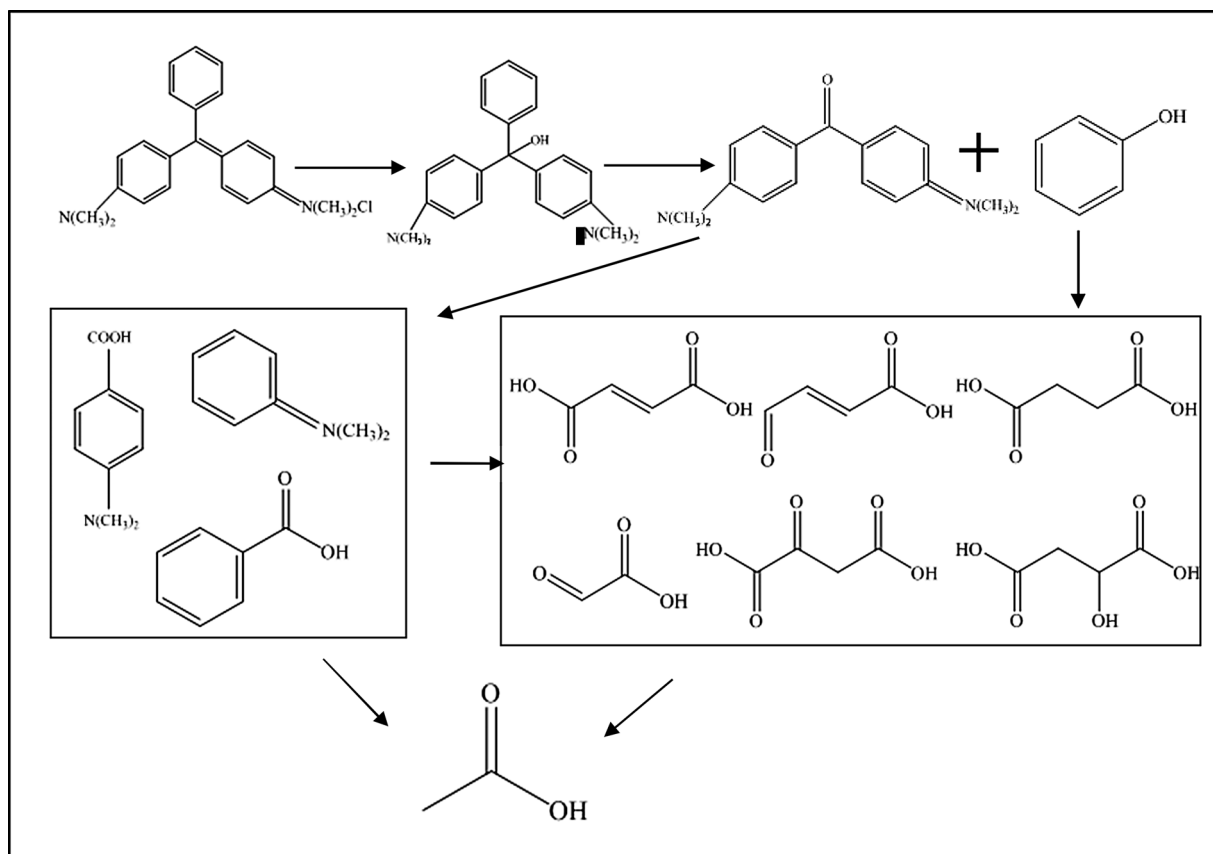
would transfer to that of  $\text{Ag}_3\text{PO}_4$  and photoinduced holes from VB of  $\text{Ag}_3\text{PO}_4$  could transfer to the VB of Cr:SrTiO<sub>3</sub>, causing the electrons and holes accumulated on the CB of  $\text{Ag}_3\text{PO}_4$  and the VB of Cr:SrTiO<sub>3</sub>, respectively. As a result, the separation and transfer process of photo-generated electron-hole pair were significantly promoted, and the recombination process was also inhibited distinctly, and finally presented as the higher photocatalytic activity. However, by this way, the photogenerated electrons in the CB of  $\text{Ag}_3\text{PO}_4$  (+0.33 eV vs. NHE, pH = 7) cannot reduce  $\text{O}_2$  into  $\cdot\text{O}_2^-$  (-0.33 eV vs. NHE, pH = 7) and the photogenerated holes on the VB of Cr:SrTiO<sub>3</sub> (+1.69 eV vs. NHE, pH = 7) also cannot react with  $\text{H}_2\text{O}$  to form  $\cdot\text{OH}$  (+2.40 V vs. NHE, pH = 7). Therefore, the general heterostructured mechanism cannot explain the separation and transfer of photoproducted electron-hole pairs of  $\text{Ag}_3\text{PO}_4$ @MWCNTs@Cr:SrTiO<sub>3</sub> composite, but instead should be explained by Z-scheme transfer mechanism. The result in Fig. 8b had proved that there was a small amount of  $\text{Ag}^0$  species formed during the irradiation processes. In this work, the metallic silver separated out from the surface of  $\text{Ag}_3\text{PO}_4$  served as photogenerated electrons and holes trappers, and could facilitate a Z-scheme transfer mechanism [18]. As presented in Fig. 11b, because of higher Schottky barriers at the metal-semiconductor interfaces, the CB potentials of  $\text{Ag}_3\text{PO}_4$  are more negative than that of metallic Ag. And the VB potentials of Cr:SrTiO<sub>3</sub> are more positive than that of metallic Ag [50,51]. Thus the photogenerated electrons in the CB of  $\text{Ag}_3\text{PO}_4$  and the photoinduced holes from the VB of Cr:SrTiO<sub>3</sub> both could transform to metallic Ag, respectively, which resulted in more efficient separation and transfer of photogenerated electron-hole pairs. Especially, the CB potentials of Cr:SrTiO<sub>3</sub> (-0.79 eV) is more negative than the  $\text{O}_2/\cdot\text{O}_2^-$  potential (-0.33 eV) and the position of VB of  $\text{Ag}_3\text{PO}_4$  (+2.59 eV) is more positive than that of  $\cdot\text{OH}/\text{OH}^-$  potential (+2.40 eV). As a consequence, the  $\text{O}_2$  molecules adsorbed on the catalyst surface could be reduced into  $\cdot\text{O}_2^-$  and the holes on the VB of  $\text{Ag}_3\text{PO}_4$  also could react with  $\text{H}_2\text{O}$  to form  $\cdot\text{OH}$ . Meanwhile, the photogenerated holes had a great affinity to capture electrons from adsorbed dye molecules, which also can oxidize MG directly. In summary, the experimental results can be well explained by Z-scheme transfer mechanism. The Z-scheme heterojunction can promote the separation of photogenerated electron-hole pairs effectively, further prolong the lifetime of charge carriers, obtain more active radicals, and finally achieve superior photocatalytic performance. As a conclusion, according to the analysis mentioned above, reactions process listed as the following may be involved:



### 3.6. Effects of MWCNTs on $\text{Ag}_3\text{PO}_4$ crystal structure and performance

Based on experimental data and characterization results, after the MWCNTs were introduced in, notable changes of the crystal size and micro-morphology of  $\text{Ag}_3\text{PO}_4$  were observed, enhanced photocatalytic activity and better photostability were also investigated (Scheme 1). The change of microstructure might be attributed to the following process. The positive charged  $\text{Ag}^+$  could easily be adsorbed by MWCNTs through electrostatic attraction with vigorous stirring for 12 h, as oxygen-containing functional groups and negatively charge on





Scheme 2. A possible photocatalytic degradation pathway of MG.

MWCNTs have previously been reported to in favor of the sorption of metal ions [52–54]. After the addition of  $\text{Na}_2\text{HPO}_4 \cdot 12\text{H}_2\text{O}$ ,  $\text{Ag}_3\text{PO}_4$  seed particles were subsequently generated and grew along the surface of MWCNT, which may in turn affect the growth of  $\text{Ag}_3\text{PO}_4$  particles. One dimensional carbon nanotubes can be regarded as seamless hollow tubes consisting of rolled graphene sheets [55], which have the potential to influence the growth process of  $\text{Ag}_3\text{PO}_4$  crystals and the final morphology formation. Moreover, the MWCNTs exhibited a significant enhancement on the photocatalytic activity for several reasons. First, high electrical conductivity along their length of MWCNTs facilitates it being an effective acceptor of the photogenerated electrons and promotes the transfer of electrons. The rapid transportation and mobility of electrons on MWCNTs efficiently keeps electrons away from the photogenerated holes, allowing more of them to react with  $\text{O}_2$  molecules and  $\text{H}^+$ , hence the enhanced degradation of pollutants. Meanwhile, sufficient time was also provided for the contact of photogenerated holes and contaminants. Benefiting from the above existing effective inhibition of charge recombination, the photocatalytic activity was accordingly elevated. Second, high aspect ratio and high surface area of the MWCNT contribute to providing more active adsorption sites and photocatalytic reaction sites, which favor the augmentation of photocatalytic performance. Third, the smaller size of the silver phosphate particles is easier to exhibit higher photocatalytic activity, which may result from the quantum size effect, surface effect, and macro quantum tunneling effect [56]. Finally, MWCNTs with abundant functional groups can readily associate with organic pollutant molecule and adsorb them through  $\pi$ – $\pi$ , electrostatic or hydrogen-bonding interactions [48,57,58]. Consequently, the pollutant molecule can be rapidly enriched on the photocatalyst surface, thus shortening the reaction time. In general, the microstructure change of  $\text{Ag}_3\text{PO}_4$  crystals was mainly due to the unique structure and physicochemical properties of MWCNTs. In addition, MWCNTs can effectively promote photocatalytic

activity and photostability of  $\text{Ag}_3\text{PO}_4$  under the efforts of all the above mentioned aspects.

### 3.7. Photocatalytic degradation products and pathway of malachite green

In order to further investigate the photodegradation products, the MG solution following 12 min reaction was detected by GC–MS. The main chemical constituents of the degraded MG were exhibited in Table S3. The major chemical components identified were some small molecular organic acids, which including acetic acid, glyoxylic acid, fumaric acid, 2-oxosuccinic acid, (E)-4-oxobut-2-enoic acid, succinic acid, benzoic acid and malic acid. According to the results above, a possible photocatalytic degradation pathway of MG were speculated and presented in Scheme 2. In the process of photodegradation, the MG molecules and intermediates will be attacked by active radicals, giving rise to a lot of complex reactions, which may involve N-demethylation reactions, benzene removal reaction and open-ring reaction, etc.

## 4. Conclusions

A novel type of Z-scheme heterojunction photocatalyst  $\text{Ag}_3\text{PO}_4 @ \text{MWCNTs} @ \text{Cr} : \text{SrTiO}_3$  was synthesized successfully and reported for the first time. The addition of MWCNTs to the composite catalyst changed the size and micro-morphology of  $\text{Ag}_3\text{PO}_4$  from a polyhedron crystal with a diameter of about  $30 \mu\text{m}$  to a spherical-like one with a diameter of  $0.28$ – $0.69 \mu\text{m}$ . The composite of  $\text{Ag}_3\text{PO}_4 @ \text{MWCNTs} @ \text{Cr} : \text{SrTiO}_3$  exhibited excellent photocatalytic activity for MG degradation in aqueous solutions under both sunlight and visible light irradiation. The active species trapping experiment and ESR analysis confirmed that  $\cdot\text{O}_2^-$  and  $\text{h}^+$  were generated in the reaction process, and there existed the Z-scheme transfer mechanisms. Several small molecular organic acids such as acetic acid, glyoxylic acid, fumaric acid and benzoic acid were



detected by GC–MS in the photodegradation products of MG, which further indicates that photocatalytic degradation pathway involved N-demethylation, benzene removal and open-ring reactions. This work provides a novel highly efficient Z-scheme heterojunction photocatalyst that can effectively utilize natural sunlight and visible light, and the discovery of change of crystal structure and properties due to adding MWCNTs offers a new strategy for preparing low-cost and efficient visible light active photocatalysts.

## Acknowledgments

This work was supported by the project of National Natural Science Foundation of China (Grant No.: 51478172, 51278464, and 51521006), the Natural Science Foundation of Zhejiang Province of China (Grant No.: LY17E080002), the Department of Science and Technology of Hunan Province of China (Contract No.: 2017JJ2029), and the Department of Science and Technology of Changsha City of China (Contract No.: kh1601187).

## Appendix A. Supplementary data

Supplementary data associated with this article can be found, in the online version, at <https://doi.org/10.1016/j.apcatb.2018.01.054>.

## References

- [1] M. Ruokolainen, E. Ollikainen, T. Sikanen, T. Kotiaho, R. Kostiainen, Oxidation of tyrosine-phosphopeptides by titanium dioxide photocatalysis, *J. Am. Chem. Soc.* 138 (2016) 7452–7455.
- [2] H.I. Villafán-Vidales, C.A. Arancibia-Bulnes, D. Riveros-Rosas, H. Romero-Paredes, C.A. Estrada, An overview of the solar thermochemical processes for hydrogen and syngas production: reactors and facilities, *Renew. Sustain. Energy Rev.* 75 (2016) 894–908.
- [3] P. Verma, Y. Kuwahara, K. Mori, H. Yamashita, Synthesis of mesoporous silica supported Ag nanorods-based bimetallic catalysts and investigation of their plasmonic activity under visible light irradiation, *Catal. Sci. Technol.* 7 (2017) 2551–2558.
- [4] H. Park, J. Choi, H. Kim, E. Hwang, D.-H. Ha, S.H. Ahn, S.-K. Kim, AgIn dendrite catalysts for electrochemical reduction of CO<sub>2</sub> to CO, *Appl. Catal. B: Environ.* 219 (2017) 123–131.
- [5] J. Angelo, P. Magalhães, L. Andrade, A. Mendes, Characterization of TiO<sub>2</sub>-based semiconductors for photocatalysis by electrochemical impedance spectroscopy, *Appl. Surf. Sci.* 387 (2016) 183–189.
- [6] M.C. Wen, K. Mori, Y. Kuwahara, T. An, H. Yamashita, Design and architecture of metal organic frameworks for visible light enhanced hydrogen production, *Appl. Catal. B: Environ.* 218 (2017) 555–569.
- [7] P. Roy, S. Berger, P. Schmuki, TiO<sub>2</sub> nanotubes: synthesis and applications, *Angew. Chem. Int. Ed.* 50 (2011) 2904–2939.
- [8] S.Q. Yu, J. Hu, J.L. Wang, Radiation-induced catalytic degradation of p-nitrophenol (PNP) in the presence of TiO<sub>2</sub> nanoparticles, *Radiat. Phys. Chem.* 79 (2010) 1039–1046.
- [9] T. Fukumura, E. Sambandan, H. Yamashita, Synthesis and VOC degradation ability of a CeO<sub>2</sub>/WO<sub>3</sub> thin-layer visible-light photocatalyst, *Mater. Res. Bull.* 94 (2017) 493–499.
- [10] Y. Bi, S. Ouyang, N. Umezawa, J. Cao, J.H. Ye, Facet effect of single-crystalline Ag<sub>3</sub>PO<sub>4</sub> sub-microcrystals on photocatalytic properties, *J. Am. Chem. Soc.* 133 (2011) 6490–6492.
- [11] X.F. Yang, H.Y. Cui, Y. Li, J. Qin, R. Zhang, H. Tang, Fabrication of Ag<sub>3</sub>PO<sub>4</sub>-graphene composites with highly efficient and stable visible light photocatalytic performance, *ACS Catal.* 3 (2013) 363–369.
- [12] Y.P. Liu, L. Fang, H.D. Lu, L.J. Liu, H. Wang, C.Z. Hu, Highly efficient and stable Ag/Ag<sub>3</sub>PO<sub>4</sub> plasmonic photocatalyst in visible light, *Catal. Commun.* 17 (2012) 200–204.
- [13] W.F. Yao, B. Zhang, C.P. Huang, C. Ma, X.L. Song, Q.J. Xu, Synthesis and characterization of high efficiency and stable Ag<sub>3</sub>PO<sub>4</sub>/TiO<sub>2</sub> visible light photocatalyst for the degradation of methylene blue and rhodamine B solutions, *J. Mater. Chem.* 22 (2012) 4050–4055.
- [14] Y. Bi, S. Ouyang, J. Cao, J.H. Ye, Facile synthesis of rhombic dodecahedral AgX/Ag<sub>3</sub>PO<sub>4</sub> (X = Cl, Br I) heterocrystals with enhanced photocatalytic properties and stabilities, *Phys. Chem. Chem. Phys.* 13 (2011) 10071–10075.
- [15] C.J. Li, P. Zhang, R. Lv, J.W. Lu, T. Wang, S.P. Wang, H.F. Wang, J.L. Gong, Photocatalysis: selective deposition of Ag<sub>3</sub>PO<sub>4</sub> on Monoclinic BiVO<sub>4</sub>(040) for highly efficient photocatalysis, *Small* 9 (2013) 3951–3956.
- [16] C.F. Mu, Y. Zhang, W.Q. Cui, Y.H. Liang, Y.F. Zhu, Removal of bisphenol A over a separation free 3D Ag<sub>3</sub>PO<sub>4</sub>-graphene hydrogel via an adsorption-photocatalysis synergy, *Appl. Catal. B: Environ.* 212 (2017) 41–49.
- [17] Y.Y. Bu, Z.Y. Chen, C.J. Sun, Highly efficient Z-Scheme Ag<sub>3</sub>PO<sub>4</sub>/Ag/WO<sub>3-x</sub> photocatalyst for its enhanced photocatalytic performance, *Appl. Catal. B: Environ.* 179 (2015) 363–371.
- [18] X.J. Guan, L.J. Guo, Cocatalytic effect of SrTiO<sub>3</sub> on Ag<sub>3</sub>PO<sub>4</sub> toward enhanced photocatalytic water oxidation, *ACS Catal.* 4 (2014) 3020–3026.
- [19] J.J. Guo, S.X. Ouyang, P. Li, Y.J. Zhang, T. Kako, J.H. Ye, A new heterojunction Ag<sub>3</sub>PO<sub>4</sub>/Cr-SrTiO<sub>3</sub> photocatalyst towards efficient elimination of gaseous organic pollutants under visible light irradiation, *Appl. Catal. B: Environ.* 134–135 (2013) 286–292.
- [20] K. Maeda, Z-scheme water splitting using two different semiconductor photocatalysts, *ACS Catal.* 3 (2013) 1486–1503.
- [21] H. Tada, T. Mitsui, T. Kiyonaga, T. Akita, K. Tanaka, All-solid-state Z-scheme in CdS-Au-TiO<sub>2</sub> three-component nanojunction system, *Nat. Mater.* 5 (2006) 782–786.
- [22] N. Srinivasan, E. Sakai, M. Miyauchi, Balanced excitation between two semiconductors in bulk heterojunction Z-scheme system for overall water splitting, *ACS Catal.* 6 (2016) 2197–2200.
- [23] R. Abe, K. Sayama, K. Domen, H. Arakawa, A new type of water splitting system composed of two different TiO<sub>2</sub> photocatalysts (anatase, rutile) and a IO<sup>3-</sup>/I<sup>-</sup> shuttle redox mediator, *Chem. Phys. Lett.* 344 (2001) 339–344.
- [24] L.L. Zhang, W.H. Feng, B. Wang, K.Q. Wang, F. Gao, Y. Zhao, P. Liu, Construction of dual-channel for optimizing Z-scheme photocatalytic system, *Appl. Catal. B: Environ.* 212 (2017) 80–88.
- [25] M. Michálek, J. Sedláček, M. Parchoviansky, M. Michálová, D. Galusek, Mechanical properties and electrical conductivity of alumina/MWCNT and alumina/zirconia/MWCNT composites, *Ceram. Int.* 40 (2014) 1289–1295.
- [26] D.H. Lin, T.T. Li, K. Yang, F.C. Wu, The relationship between humic acid (HA) adsorption on and stabilizing multiwalled carbon nanotubes (MWNTs) in water: effects of HA MWNT and solution properties, *J. Hazard. Mater.* 241–242 (2012) 404–410.
- [27] J. Fang, M.H. Wang, B. Shen, L.Q. Zhang, D.H. Lin, Distinguishable co-transport mechanisms of phenanthrene and oxytetracycline with oxidized-multiwalled carbon nanotubes through saturated soil and sediment columns: vehicle and competition effects, *Water Res.* 108 (2016) 271–279.
- [28] X.T. Wang, L. Cai, P. Han, D.H. Lin, H.J. Kim, M.P. Tong, Cotransport of multi-walled carbon nanotubes and titanium dioxide nanoparticles in saturated porous media, *Environ. Pollut.* 195 (2014) 31–38.
- [29] Z. Wang, Y. Lu, M. Zhang, G.W. Zhou, H. Fei, H.X. Shi, H.J. Dai, Synthesis and characterization of Ag<sub>3</sub>PO<sub>4</sub>/multiwalled carbon nanotube composite photocatalyst with enhanced photocatalytic activity and stability under visible light, *J. Mater. Sci.* 49 (2014) 1585–1593.
- [30] L. Cai, X. Xiong, N.G. Liang, Q.Y. Long, Highly effective and stable Ag<sub>3</sub>PO<sub>4</sub>-WO<sub>3</sub>/MWCNTs photocatalysts for simultaneous Cr(VI) reduction and orange II degradation under visible light irradiation, *Appl. Surf. Sci.* 353 (2015) 939–948.
- [31] S.M. Wang, D.L. Li, C. Sun, S.G. Yang, Y. Guan, H. He, Highly efficient photocatalytic treatment of dye wastewater via visible-light-driven AgBr-Ag<sub>3</sub>PO<sub>4</sub>/MWCNTs, *J. Mol. Catal. A: Chem.* 383–384 (2014) 128–136.
- [32] S.X. Ouyang, H. Tong, N. Umezawa, J.Y. Cao, P. Li, Y.P. Bi, Y.J. Zhang, J.H. Ye, Surface-alkalinization-induced enhancement of photocatalytic H<sub>2</sub> evolution over SrTiO<sub>3</sub>-based photocatalysts, *J. Am. Chem. Soc.* 134 (2012) 1974–1977.
- [33] S. Tonda, S. Kumar, O. Anjaneyulu, V. Shanker, Synthesis of Cr and La-Codoped SrTiO<sub>3</sub> nanoparticles for enhanced photocatalytic performance under sunlight irradiation, *Phys. Chem. Chem. Phys.* 16 (2014) 23819–23828.
- [34] G. Chiarotti, Optical properties of solids, *Phys. Today* 26 (1973) 60–61.
- [35] S.K.J. Al-Ani, K.I. Arshak, C.A. Hogarth, The optical absorption edge of amorphous thin films of silicon monoxide, *J. Mater. Sci.* 19 (1984) 1737–1748.
- [36] Adrian W. Bott, Electrochemistry of semiconductors, *Curr. Sep.* 17 (1998) 87–91.
- [37] Y. Matsumoto, Energy positions of oxide semiconductors and photocatalysis with iron complex oxides, *J. Solid State Chem.* 126 (1996) 227–234.
- [38] Y.C. Deng, L. Tang, G.M. Zeng, Z.J. Zhu, M. Yan, Y.Y. Zhou, J.J. Wang, Y.N. Liu, J.J. Wang, Insight into highly efficient simultaneous photocatalytic removal of Cr(VI) and 2,4-dichlorophenol under visible light irradiation by phosphorus doped porous ultrathin g-C<sub>3</sub>N<sub>4</sub> nanosheets from aqueous media: performance and reaction mechanism, *Appl. Catal. B: Environ.* 203 (2017) 343–354.
- [39] Z.G. Yi, J.H. Ye, N. Kikugawa, T. Kako, S. Ouyang, H. Yang, J. Cao, W. Luo, Z. Li, An orthophosphate semiconductor with photooxidation properties under visible-light irradiation, *Nat. Mater.* 9 (2010) 559.
- [40] X.J. Chen, Y.Z. Dai, X.Y. Wang, Methods and mechanism for improvement of photocatalytic activity and stability of Ag<sub>3</sub>PO<sub>4</sub>: a review, *J. Alloys Compd.* 649 (2015) 910–932.
- [41] D.J. Wang, Z.H. Li, L.W. Shang, J.W. Liu, J. Shen, Heterostructured Ag<sub>3</sub>PO<sub>4</sub>/TiO<sub>2</sub> film with high efficiency for degradation of methyl orange under visible light, *Thin Solid Films* 551 (2014) 8–12.
- [42] Z.Y. Zhang, D.L. Jiang, D. Li, M.Q. He, M. Chen, Construction of SnNb<sub>2</sub>O<sub>6</sub> nanosheet/g-C<sub>3</sub>N<sub>4</sub> nanosheet two-dimensional heterostructures with improved photocatalytic activity: synergistic effect and mechanism insight, *Appl. Catal. B: Environ.* 183 (2016) 113–123.
- [43] T. Cai, Y.T. Liu, L.L. Wang, S.Q. Zhang, Y.X. Zeng, J.L. Yuan, J.H. Ma, W.Y. Dong, C.B. Liu, S.L. Luo, Silver phosphate-based Z-scheme photocatalytic system with superior sunlight photocatalytic activities and anti-photocorrosion performance, *Appl. Catal. B: Environ.* 208 (2017) 1–13.
- [44] S.Q. Liu, S. Cheng, L.R. Feng, X.M. Wang, Z.G. Chen, Effect of alkali cations on heterogeneous photo-Fenton process mediated by Prussian blue colloids, *J. Hazard. Mater.* 182 (2010) 665–671.
- [45] A.J. Machulek, J.E. Moraes, C. Vautiergiongo, C.A. Silverio, L.C. Friedrich, C.A. Nascimento, M.C. Gonzalez, F.H. Quina, Abatement of the inhibitory effect of chloride anions on the photo-Fenton process, *Environ. Sci. Technol.* 41 (2007) 8459–8463.
- [46] B. Samiey, A.R. Toosi, Adsorption of malachite green on silica gel: effects of NaCl,

- pH and 2-propanol, *J. Hazard. Mater.* 184 (2010) 739–745.
- [47] F. Chen, Q. Yang, X.M. Li, G.M. Zeng, D.B. Wang, C.G. Niu, J.W. Zhao, H.X. An, T. Xie, Y.C. Deng, Hierarchical assembly of graphene-bridged  $\text{Ag}_3\text{PO}_4/\text{Ag}/\text{BiVO}_4$  (040) Z-Scheme photocatalyst: an efficient sustainable and heterogeneous catalyst with enhanced visible-light photoactivity towards tetracycline degradation under visible light irradiation, *Appl. Catal. B: Environ.* 200 (2017) 330–342.
- [48] Y.H. Tu, C.P. Yang, C. Yan, G.M. Zeng, L. Li, W. Lu, Effect of saponins on n-hexane removal in biotrickling filters, *Bioresour. Technol.* 175 (2015) 231–238.
- [49] H.L. Lin, J. Cao, B.D. Luo, B.Y. Xu, S.F. Chen, Synthesis of novel Z-scheme  $\text{AgI}/\text{Ag}/\text{AgBr}$  composite with enhanced visible light photocatalytic activity, *Catal. Commun.* 21 (2012) 91–95.
- [50] F. Chen, Q. Yang, Y.L. Wang, J.W. Zhao, D.B. Wang, X.M. Li, Z. Guo, H. Wang, Y.C. Deng, C.G. Niu, G.M. Zeng, Novel ternary heterojunction photocatalyst of Ag nanoparticles and g- $\text{C}_3\text{N}_4$  nanosheets co-modified  $\text{BiVO}_4$  for wider spectrum visible-light photocatalytic degradation of refractory pollutant, *Appl. Catal. B: Environ.* 205 (2017) 133–147.
- [51] J.L. Wang, Z.Y. Bai, Fe-based catalysts for heterogeneous catalytic ozonation of emerging contaminants in water and wastewater, *Chem. Eng. J.* 312 (2017) 79–98.
- [52] D.H. Lin, X.L. Tian, T.T. Li, Z.Y. Zhang, X. He, B.S. Xing, Surface-bound humic acid increased  $\text{Pb}^{2+}$  sorption on carbon nanotubes, *Environ. Pollut.* 167 (2012) 138–147.
- [53] X.L. Tian, T.T. Li, K. Yang, Y. Xu, H.F. Lu, D.H. Lin, Effect of humic acids on physicochemical property and  $\text{Cd}(\text{II})$  sorption of multiwalled carbon nanotubes, *Chemosphere* 89 (2012) 1316–1322.
- [54] C.P. Yang, H. Chen, G.M. Zeng, G.L. Yu, S.L. Luo, Biomass accumulation and control strategies in gas biofiltration, *Biotechnol. Adv.* 28 (2010) 531–540.
- [55] H.F. Hu, Y.P. Song, M. Feng, H.B. Zhan, Carbon nanomaterials for simultaneous determination of dopamine and uric acid in the presence of ascorbic acid: from one-dimensional to the quasi one-dimensional, *Electrochim. Acta* 190 (2016) 40–48.
- [56] A.I. Ekimov, A.L. Efros, A.A. Onushchenko, Quantum size effect in semiconductor microcrystals, *Solid State Commun.* 56 (1993) 921–924.
- [57] Y. Cheng, H.J. He, C.P. Yang, G.M. Zeng, X. Li, H. Chen, G.L. Yu, Challenges and solutions for biofiltration of hydrophobic volatile organic compounds, *Biotechnol. Adv.* 34 (2016) 1091–1102.
- [58] A.M. Cassell, J. Li, R.M.D. Stevens, J.E. Koehne, Vertically aligned carbon nanotube heterojunctions, *Appl. Phys. Lett.* 85 (2004) 2364–2366.